Redox evolution during arc magma differentiation revealed by mineral/melt Fe3+ and Fe2+ partitioning

Fangfang Huang (huangfangfang@gig.ac.cn)
State Key Laboratory of Isotope Geochemistry, Guangzhou Institute of Geochemistry, Chinese Academy of Sciences

Jintuan Wang (wangjt@gig.ac.cn)
Guangzhou Institute of Geochemistry, Chinese Academy of Sciences, Guangzhou

Xiaolin Xiong (xiongxl@gig.ac.cn)

Article

Keywords:

DOI: https://doi.org/10.21203/rs.3.rs-1540804/v2

Additional Declarations: There is **NO** Competing Interest.

Redox evolution during arc magma differentiation revealed by mineral/melt Fe^{3+} and Fe^{2+} partitioning

Abstract

The oxidizing capacity of volcanic gases relies on both the redox state of the mantle and the redox evolution of mantle-derived magmas. Arc magmas transfer abundant volatiles from the mantle and undergo extensive differentiation before degassing. But how the magmatic redox state evolves during differentiation remains enigmatic. The redox evolution of a magma depends on the mineral/melt partition coefficients of Fe^{3+} and Fe^{2+} (DFe^{3+} and DFe^{2+}). However, no systematic DFe^{3+} and DFe^{2+} are reported due to the difficulties in analyzing Fe^{3+} of silicate minerals. Here, we conducted hydrous experiments at 900−1100 °C and 1−2 GPa and determined systematically DFe^{3+} and DFe^{2+} using a novel method. With the obtained partition coefficients, we investigated the redox evolution by performing fractional crystallization modelling. The almost invariable redox state during arc magma differentiation implies an oxidizing mantle predated the Great Oxidation Event if it was triggered by the increasing oxidizing capacity of volcanic gases.

The Earth's mantle regulates the secular evolution of the atmosphere by dominating the redox state (described by oxygen fugacity, fO_2) of mantle-derived magmas and emanated volatiles therein[1-4]. Arc magmas, deriving from sub-arc mantle, contain abundant volatiles[5,6] and may undergo extensive differentiation from basaltic, through andesitic and dacitic, to rhyolitic compositions on the way to eruption[7-9]. Differentiation may significantly affect the fO_2 of the erupted magmas and the oxidizing capacity of the expelled volatiles, and thus augment or abate the capacity of the mantle in regulating the atmospheric compositions. But how and if fO_2 evolves during arc magma differentiation remains hotly debated. Some studies suggest that arc magmas beneath thick crust will be continuously oxidized due to garnet fractionation, which increases

the Fe^{3+}/Fe_T ratio of the residual melt because garnet prefers Fe^{2+} over Fe^{3+} [10,11]. Other studies suggest, based on mineral oxybarometer or direct analysis of melt Fe^{3+}/Fe_T ratios, that the fO_2 of arc magmas remains nearly constant during magmatic differentiation, regardless of the crustal thickness[12-16]. The debate arises mainly from the lack of mineral/melt partition coefficients of Fe^{3+} and Fe^{2+} during arc magma differentiation.

Iron is the most abundant multivalent elements on Earth and the magmatic fO_2, reflected by the Fe^{3+}/Fe_T ($Fe_T = Fe^{3+} + Fe^{2+}$) ratio of the magma, is thus largely controlled by the behavior of ferric (Fe^{3+}) and ferrous (Fe^{2+}) iron[17,18]. In a closed magmatic system, crystallization of Fe-bearing minerals will fractionate the Fe^{3+}/Fe^{2+} (i.e. Fe^{3+}/Fe_T) ratio of the magma and change the fO_2 of the system[19]. Specifically, fractional crystallization of a mineral that preferentially partitions Fe^{2+} over Fe^{3+} (i.e. $DFe^{3+}/DFe^{2+}<1$, DFe^{3+} and DFe^{2+} are the mineral/melt Fe^{3+} and Fe^{2+} partition coefficients) will impart a higher Fe^{3+}/Fe^{2+} ratio on the residual melt, resulting in an elevated fO_2 of the system, and vice versa. Therefore, constraints on DFe^{3+}, DFe^{2+} and DFe^{3+}/DFe^{2+} for the major crystallizing minerals and their equilibrium melts are essential in deciphering the redox evolution during arc magma differentiation.

The major Fe-bearing minerals during arc magma differentiation include olivine (ol), clinopyroxene (cpx), amphibole (amp), garnet (grt) and Fe-oxides. The DFe^{2+} for these minerals can be determined by performing high pressure experiments at reducing conditions where Fe is almost present exclusively as Fe^{2+} [20,21]. Most published reducing experiments are buffered by graphite, where Fe^{2+}/Fe_T ratios exceed 0.95−0.98[22-25]. Therefore, the bulk iron partition coefficient (DFe_T) obtained from the very reducing experiments can approximately represent DFe^{2+}. For the case of DFe^{3+}, it approximates 0 for ol because ol contains negligible Fe^{3+} due to the steric limitations in the crystal structure[26]. For Fe-oxides, [magnetite (mag) and spinel (spl)], the DFe^{3+} can be readily determined because the mineral Fe^{3+} content can be accurately calculated from the mineral composition determined, e.g. by electron microprobe[21,27]. However, DFe^{3+} for silicate minerals (cpx, amp and grt) are only sporadically reported[21,28-30] and the results are inapplicable to arc magma differentiation because the experiments were performed

at dry or high temperature (>1100 °C) conditions. The lack of systematic DFe^{3+} for silicate minerals at conditions pertinent to arc magma differentiation mainly results from the following difficulties. Firstly, the proportion of Fe^{3+} rarely exceeds 0.8 in high pressure experiments[18,31]; secondly, Fe^{3+} analysis of hydrous silicate melts remains a difficult task[32]; thirdly, unlike for Fe-oxides, the Fe^{3+} content of silicate minerals cannot be accurately calculated from their composition[26]; at last, an accurate analytical method for determining Fe^{3+} in silicate minerals by X-ray absorption near edge structure (XANES) remains to be established, especially for anisotropic minerals such as pyroxenes[33].

Here, we performed high temperature and pressure (HTP) experiments and determined DFe^{3+} for silicate minerals (cpx, amp, grt) with high precision following a novel method. The method circumvents the above difficulties by determining DFe^{3+} according to the relation: $DFe^{3+}=\frac{DFe_T-DFe^{2+}}{(Fe^{3+}/Fe_T)^{melt}}+DFe^{2+}$. The HTP experiments were performed in a piston-cylinder apparatus at 900−1100 °C and 1−2 GPa (Supplementary Table 1), covering the typical T−P ranges of arc magma differentiation (cf. [9,34]). The obtained partition coefficients can thus be directly applied to constrain the redox evolution during arc magma differentiation.

Determination of DFe^{3+} from a novel method

DFe^{3+} can be determined according to the following equation (details for the derivation of the equation are reported in the SI text):

$$DFe^{3+}=\frac{DFe_T-DFe^{2+}}{(Fe^{3+}/Fe_T)^{melt}}+DFe^{2+} \qquad (1)$$

Equation (1) indicates that DFe^{3+} can be obtained when DFe_T, DFe^{2+} and melt Fe^{3+}/Fe_T $[(Fe^{3+}/Fe_T)^{melt}]$ are accurately constrained. For an experiment with known fO_2, DFe_T is readily determined by analyzing the FeO_T content of the minerals and coexisting melt, while $(Fe^{3+}/Fe_T)^{melt}$ can be calculated from the experimental fO_2, temperature, pressure, and melt compositions using well-calibrated equations[17,18]. Therefore, we can determine DFe^{3+} when DFe^{2+} is precisely constrained and measured.

According to equation (1), the propagated uncertainty of DFe^{3+} can be expressed by the following equation:

$$\delta DFe^{3+}=\sqrt{\left(\frac{1}{(Fe^{3+}/Fe_T)^{melt}}\right)^2*(\delta DFe_T)^2+\left(1-\frac{1}{(Fe^{3+}/Fe_T)^{melt}}\right)^2*(\delta DFe^{2+})^2+\frac{(DFe_T-DFe^{2+})^2}{(Fe^{3+}/Fe_T)^{melt^4}}*(\delta(Fe^{3+}/Fe_T)^{melt})^2} \quad (2)$$

Where δ represents the standard error of each variable (e.g., δDFe_T denotes the S.E. of DFe_T). As shown in equation (2), the S.E. of DFe^{3+} acquired by this method mainly depends on the accuracy of the $(Fe^{3+}/Fe_T)^{melt}$ value because DFe_T and DFe^{2+} can be accurately determined. With equations (1) and (2), we tested the effect of $(Fe^{3+}/Fe_T)^{melt}$ on the accuracy of DFe^{3+} assuming that DFe_T=3±0.2 and DFe^{2+}=2±0.2 and the S.E. of $(Fe^{3+}/Fe_T)^{melt}$ varies from 0.05 to 0.1. The calculated DFe^{3+} and the propagated uncertainty are shown in Fig. 1. It is evident that the lower S.E. in $(Fe^{3+}/Fe_T)^{melt}$ always results in lower S.E. of DFe^{3+} (Fig. 1A). More importantly, at a given S.E. of $(Fe^{3+}/Fe_T)^{melt}$, the S.E. of DFe^{3+} decreases dramatically with increasing $(Fe^{3+}/Fe_T)^{melt}$ and the relative uncertainty is < 10% at $(Fe^{3+}/Fe_T)^{melt}$ > ~0.7 (Fig. 1B). The dramatic decrease in the S.E. of DFe^{3+} with increasing $(Fe^{3+}/Fe_T)^{melt}$ indicates that DFe^{3+} can be accurately determined at highly oxidizing conditions (e.g., S.E.<10% at Ru−RuO_2 buffered conditions as in this study).

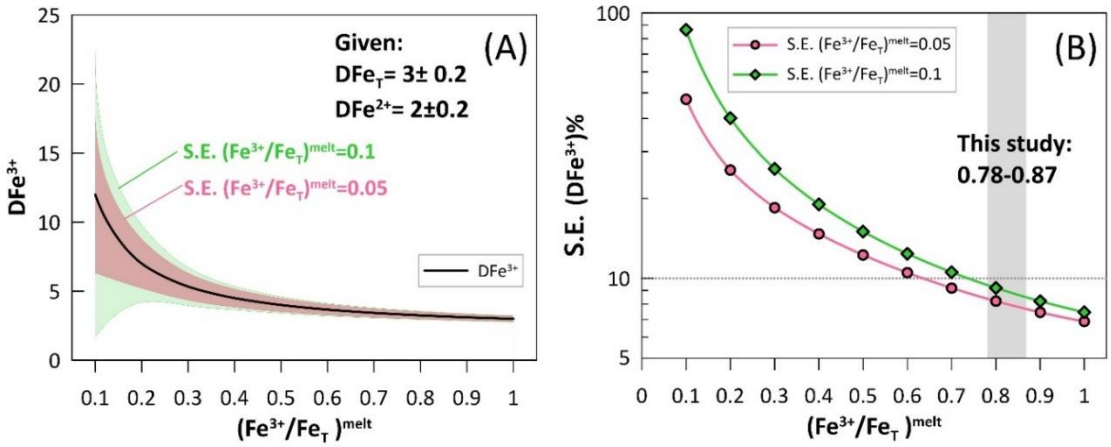

Fig. 1. Schematic diagram showing the effect of $(Fe^{3+}/Fe_T)^{melt}$ on the propagated standard error (S.E.) of DFe^{3+} for DFe_T=3±0.2 and DFe^{2+}=2±0.2. (**A**) The effect of $(Fe^{3+}/Fe_T)^{melt}$ on the absolute S.E. of DFe^{3+}. The black curve represents the calculated DFe^{3+}. The trumpet-shaped coloured areas denote the absolute S.E. of DFe^{3+} assuming an S.E. of 0.05 (circle-filled) and 0.10 (diamond-filled) for $(Fe^{3+}/Fe_T)^{melt}$. (**B**) The effect of $(Fe^{3+}/Fe_T)^{melt}$ on the relative S.E. of DFe^{3+}. The grey shaded area highlights the $(Fe^{3+}/Fe_T)^{melt}$ range of our experiments, suggesting that the S.E. of DFe^{3+} calculated from equation (1) is <10% relative. Note that change the DFe_T and DFe^{2+} could change the absolute values of the calculated DFe^{3+} and S.E., but will not affect the general trend of the DFe^{3+} and S.E..

Regression of DFe^{2+} from reducing experiments

For ferromagnesian minerals, DFe^{2+} can be expressed by DMg (magnesium partition coefficient) following the relation: $DFe^{2+} = a*DMg + b$, where a and b are constants[35,36]. We here confirmed that amphibole conforms to this relation because the ratio of DFe^{2+} and DMg ($Kd^{amp/melt}_{Fe^{2+}\text{-}Mg}$) never changes with temperature, pressure or mineral compositions (see Fig. S1 and Supplementary Text). At reducing conditions, where iron is almost exclusively present as Fe^{2+}, DFe_T is approximated by DFe^{2+}, thus enabling us to determine the relation between DFe^{2+} and DMg.

To determine the relation between DFe^{2+} and DMg for amp, we collected amphibole–melt pairs from HTP experiments and picked out the experiments performed under reducing conditions for the regression[9,28,34,37,38]. The criteria for the filtration of the experiments were: 1) we preferred experiments performed in graphite capsules because iron was mainly present as Fe^{2+} (with melt $Fe^{2+}/Fe_T > 0.95$)[22-25]; 2) for experiments performed in noble metals capsules, we calculated the $(Fe^{3+}/Fe_T)^{melt}$ from the reported fO_2 using the algorithms of Zhang et al.[18] or from the coexisting ol-melt pair using the ol- oxybarometry of Blundy et al.[20] and then chose the experiments with the calculated $(Fe^{3+}/Fe_T)^{melt}$ <0.1. Finally, 36 experiments met the criteria (Supplementary Table 2), which were regressed to obtain the following equation:

$$\text{Amp: } DFe^{2+} = 0.2919*DMg+0.0460 \quad (n=36, aad=0.14, R^2=0.81) \quad (3)$$

Where aad is the average absolute deviation. Details for the regression are reported in Fig. S2. For cpx and grt, the relations between DFe^{2+} and DMg are from a related manuscript:

$$\text{Cpx: } DFe^{2+} = 0.3822*DMg-0.0287*DMg^2 \quad (n=126, aad=0.06, R^2=0.85) \quad (4)$$

$$\text{Grt: } DFe^{2+} = 0.5843*DMg-0.1210 \quad (n=44, aad=0.09, R^2=0.99) \quad (5)$$

P–values for DMg in the regressions are far less than 0.05. The high R^2 and low S.D. demonstrate the reliability and accuracy of the parameterized equations.

Results

Twelve experiments were successfully synthesized at 900−1100 °C, 1−2 GPa and Ru–RuO_2 buffered conditions (see later Materials and Methods part and Supplementary Table 1). Both Ru and RuO_2 present at the end of each experiment (Fig. 2), indicating the validity of the fO_2 buffer. The experimental run products include melt, clinopyroxene, amphibole, garnet and Fe-oxides. The melts usually quenched to clear glasses with some of them containing tiny (usually < 3 μm) vesicles caused by H_2O exsolution during quenching. The minerals were generally euhedral with crystal sizes varying from <10−15 μm (clinopyroxene, amphibole and Fe-oxides) to up to 50 μm (garnet) (Fig. 2).

Melt compositions and $(Fe^{3+}/Fe_T)^{melt}$

The quenched melts are compositionally homogeneous (Supplementary Table 3). On an anhydrous basis, melts from the 1.0 GPa experiments are basaltic-andesitic to andesitic (55.16−62.97% SiO_2) and those from the 2.0 GPa experiments are andesitic to dacitic (61.85−67.38% SiO_2). At each pressure, melt SiO_2 and K_2O increase, but MgO and FeO_T decrease with temperature decreasing from 1100 °C to 900 °C. Because metallic Ru and RuO_2 coexist after the experiments, the experimental fO_2 can be accurately calculated using the algorithm of O'Neill and Nell[39]. The calculated $\log_{10}(fO_2)$ ranges from −5.23 to −2.71 and the relative fO_2 varies from FMQ+5.4 to FMQ+6.4 (FMQ, the fayalite–magnetite–quartz buffer[40]).

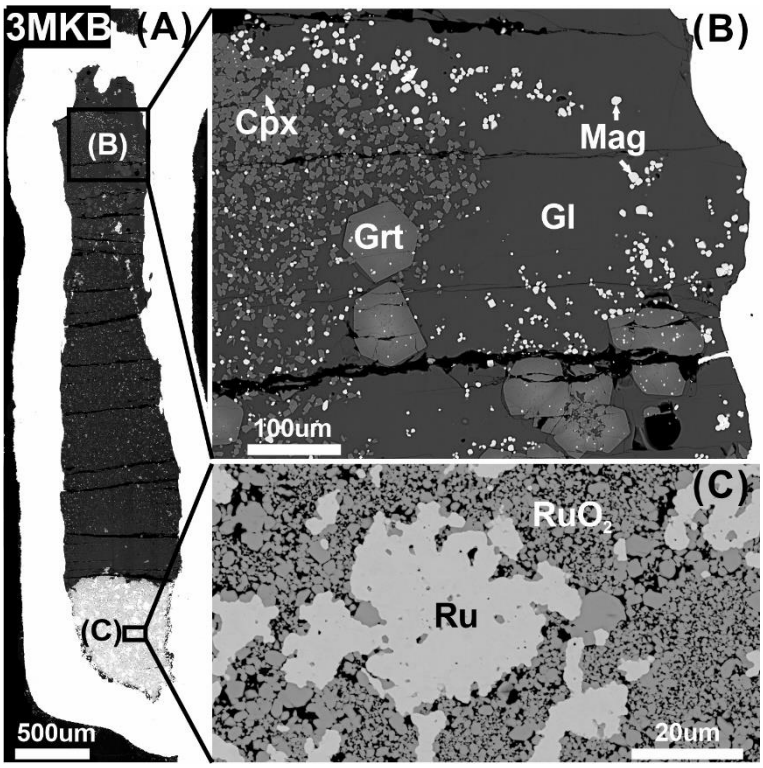

Fig. 2. Representative BSE images showing the run products of Exp. 3MKB. (**A**) An overview of the longitudinal section of the sample capsule. (**B**) An enlarged image showing the euhedral minerals and coexisting quenched glass. (**C**) The coexistence of Ru and RuO_2 indicating the validity of the fO_2 buffer. Abbreviations: Grt, garnet; Cpx, clinopyroxene; Mag, magnetite; Gl, quenched glass.

The $(Fe^{3+}/Fe_T)^{melt}$ can be calculated from the experimental fO_2, temperature, pressure and melt composition using the well-calibrated algorithms[17,18,41]. The compositional effect in O'Neill et al.[41], which is inherited from Jayasuriya et al.[42], may be inaccurate by overestimating the effects of P_2O_5[43,44]. Therefore, we calculated $(Fe^{3+}/Fe_T)^{melt}$ using the algorithms of Kress and Carmichael[17] (equation A−6) and Zhang et al.[18] (equation 10−b), respectively. The $(Fe^{3+}/Fe_T)^{melt}$ calculated by these two methods agree with each other within an error of ±0.05 (Fig. S3), indicating their reliability. In keeping with related manuscript, here we adopt the $(Fe^{3+}/Fe_T)^{melt}$ calculated using the algorithm of Zhang et al.[18]. The calculated $(Fe^{3+}/Fe_T)^{melt}$ values range from 0.73 to 0.85, showing a slight increase with decreasing temperature and pressure. Considering that the difference in the calculated $(Fe^{3+}/Fe_T)^{melt}$ from the Kress

and Carmichael[17] and the Zhang et al.[18] algorithms is <0.05, we employed an absolute uncertainty of 0.05 for the calculated $(Fe^{3+}/Fe_T)^{melt}$ in the following calculations. The calculated CFe^{3+} and CFe^{2+} in melt ranges from 1.18−4.28 wt% and 0.19−1.09 wt%, respectively. Considering Fe^{3+} as a network-forming cation, the calculated melt NBO/T (degree of depolymerization) values range from 0.02 to 0.38.

Mineral compositions

The mineral compositions of cpx, amp and Fe-oxides from single experiments are homogeneous, indicating the attainment of equilibrium. Although garnet zonation occurs in some experiments, the garnet rims should approach equilibrium with the coexisting melts as confirmed by their homogeneous compositions. Therefore, the compositions of garnet rim and the adjacent melt were used in subsequent calculations of the partition coefficients (Supplementary Table 3).

Cpx occurs in both 1 and 2 GPa experiments. Crystals have $En_{36.3–49.3}Fs_{6.5–17.4}Wo_{44.2–48.5}$ (En, enstatite; Fs, ferrosilite; Wo, wollastonite), containing 3.32−11.73 wt % Al_2O_3 and < 3.3 wt % Na_2O. The cpx from Exp. 11MKB (1 GPa, 1000 °C) splits into two distinct compositional groups: one (h-Al) is high in Al_2O_3 and FeO_T (Al_2O_3=6.14 wt%; FeO_T=6.56 wt%) and the other (l-Al) is low in Al_2O_3 and FeO_T (Al_2O_3=3.32 wt%; FeO_T=4.12 wt%). The distinct compositions in cpx are commonly recognized in both experimental and natural samples[9,45-47]. As demonstrated by Welsch et al.[48], such compositional differences represent different crystal orientations rather than disequilibrium. Amp also occurs in both 1 and 2 GPa experiments, classifiying as pargasite or magnesio-hastingsite[49,50]. FeO_T and Al_2O_3 contents in amps range from 6.54 wt% to 8.56 wt% and 14.03 to 17.07 wt%, respectively. Grt occurs only in the 2 GPa runs and they are dominantly composed of $Pyr_{63.0–68.3}Grs_{13.8–17.4}Alm_{4.9–7.8}And_{2.1–4.2}Spe_{6.7–10.1}$ (Pyr, pyrope; Grs, grossular; Alm, almandine; And, andradite; Spe, spessartite). Their FeO content increases systematically from 4.76 wt% at 900 °C to 6.52 wt% at 1100 °C. Fe-oxides occur in all of the experiments and classifying as magnetite and spinel. The magnetite and spinel crystals are composed of $Spl_{0.4–0.8}Her_{4.7–12.4}Mfr_{4.3–7.6}Mag_{65.6–75.5}Chr_{2.6–6.3}Usp_{7.2–8.8}$ and $Spl_{10.7–32.1}Her_{4.2–10.4}$

$Mfr_{27.7–48.8}Mag_{8.9–19.8}Chr_{2.1–2.9}Usp_{0.0–0.1}$, respectively (Spl, spinel; Her, hercynite; Mfr, magnesioferrite; Mag, magnetite; Chr, chromite; Usp, ulvöspinel)[51]. Mag contains 4.9−6.2 wt% TiO_2, 1.1–1.9 wt% MgO and 2.1−5.76 wt% Al_2O_3, and Spl contains ~0.2−0.4 wt% TiO_2, 12.3–13.8 wt % MgO and 7.7−25.6 wt% Al_2O_3.

DFe_T, DFe^{2+}, DFe^{3+}, and DFe^{3+}/DFe^{2+} for minerals

DFe_T for both silicate minerals and Fe-oxides were determined by dividing the FeO_T content of the minerals by that of the coexisting melts. For silicate minerals (cpx, amp and grt), the DFe^{2+} values were calculated from the relations between DFe^{2+} and DMg [Eqs. (3)−(5)] and DFe^{3+} values were then calculated from DFe_T, DFe^{2+} and $(Fe^{3+}/Fe_T)^{melt}$ using equation (1). For Fe-oxides (mag and spl), we directly calculated FeO and Fe_2O_3 contents of the minerals based on the charge balance of chemical formula, and then DFe^{2+} and DFe^{3+} were respectively determined by dividing the FeO and Fe_2O_3 contents of the minerals by those of the melts. We also verified the accuracy of the DFe^{3+} by calculating it using the $(Fe^{3+}/Fe_T)^{melt}$ obtained respectively from Kress and Carmichael[17] (equation A−6) and Zhang et al.[18]. The excellent agreement (fig. S4) demonstrated the accuracy of the determined DFe^{3+}. Additionally, the DFe^{3+}/DFe^{2+} for each mineral was calculated from the conjugated DFe^{3+} and DFe^{2+}. With the above methods, we also calculated the DFe^{2+}, DFe^{3+} and DFe^{3+}/DFe^{2+} from the oxidizing experiments of King et al.[28], Sorbadere et al.[52] and Davis and Cottrell [21], and reported DFe^{2+}, DFe^{3+} and DFe^{3+}/DFe^{2+} from Mallmann and O'Neill[29] for comparison (Supplementary Table 4).

Cpx from this study shows ranges of 0.23−3.19 for DFe_T, 0.88−1.27 for DFe^{2+}, 0.98−6.28 for DFe^{3+}, and 1.00−6.11 for DFe^{3+}/DFe^{2+}, respectively (Supplementary Table 4a). Generally, DFe_T, DFe^{2+}, DFe^{3+} and DFe^{3+}/DFe^{2+} all decrease with temperature (T) and melt NBO/T as exhibited by both our experiments and literature data (Fig. 3A−B). In addition, DFe^{3+} and DFe^{3+}/DFe^{2+} increase with the DAl (partition coefficient of Al_2O_3) (Fig. 3C−D). Considering the effects of T, NBO/T and DAl, our results are consistent with literature data regardless of the pressure. Importantly, the DFe^{3+}/DFe^{2+} for cpx is always ≥1, indicating that the crystallization of cpx will lower

Fe^{3+}/Fe_T ratio and fO_2 of the residual melt. Because the NBO/T and temperature are positively correlated, we regressed DFe^{3+}/DFe^{2+} using temperature and DAl for the convenience of subsequent redox modelling and obtained the following equation:

Cpx: $DFe^{3+}/DFe^{2+}=-8.8638+4.9634*DAl+11898/T$, n=23, $R^2=0.76$ (6)

In the regression, we only used data from this study and related manuscript because D-values from these two studies were determined using the same method. P-values for each parameter are far less than 0.05. The small P-values and relatively high R^2 indicate the reliability and accuracy of the regression.

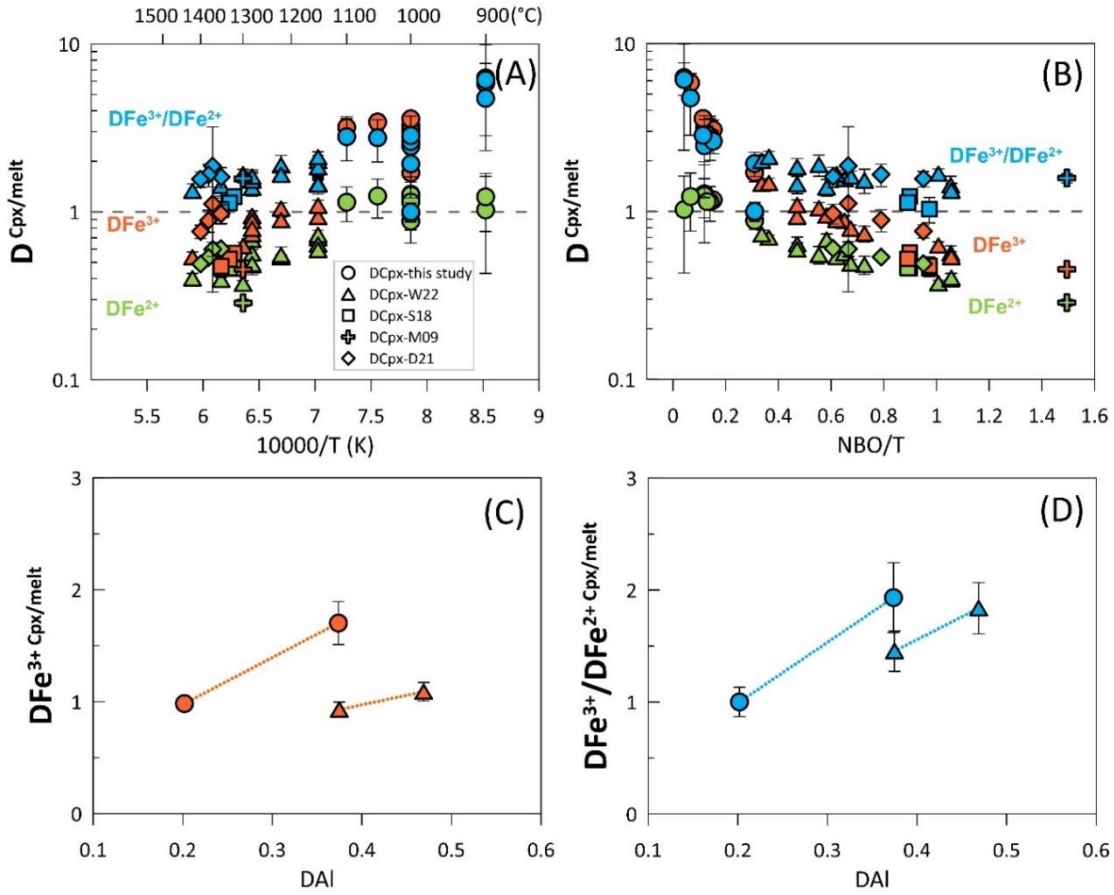

Fig. 3. DFe^{3+}, DFe^{2+} and DFe^{3+}/DFe^{2+} for cpx and melt. (**A**) DFe^{3+}, DFe^{2+} and DFe^{3+}/DFe^{2+} as a function of 10000/T. (**B**) DFe^{3+}, DFe^{2+} and DFe^{3+}/DFe^{2+} as a function of melt NBO/T. (**C**) DFe^{3+} vs. DAl. (**D**) DFe^{3+}/DFe^{2+} vs. DAl. Data cited are from W22: related manuscript, S18: Sorbadere et al.[52], M09: Mallmann & O'Neill[29] and D21: Davis et al.[21].

Amp shows ranges of 2.80−5.01 for DFe_T, 1.73−4.39 for DFe^{2+}, 2.85−5.11 for DFe^{3+} and 1.10−1.80 for DFe^{3+}/DFe^{2+} at our experimental conditions (Supplementary Table 4b). Similar to cpx, the DFe_T, $DFe^{2+}$and DFe^{3+} decrease with T and melt NBO/T (Fig. 4A−B). But the effects of T and NBO/T on DFe^{3+}/DFe^{2+} of Amp are indiscernible.

We note that the DFe^{3+}/DFe^{2+} values calculated from the most oxidizing experiment of King et al.[28] is generally consistent with our results. Here we propose an average DFe^{3+}/DFe^{2+} of 1.38 from our experiments.

$$\text{Amp: } DFe^{3+}/DFe^{2+}=1.38\ (\pm 0.31) \quad (7)$$

Because the DFe^{3+}/DFe^{2+} is always >1, similar to cpx, amp crystallization will lower Fe^{3+}/Fe_T and fO_2 of the residual melt.

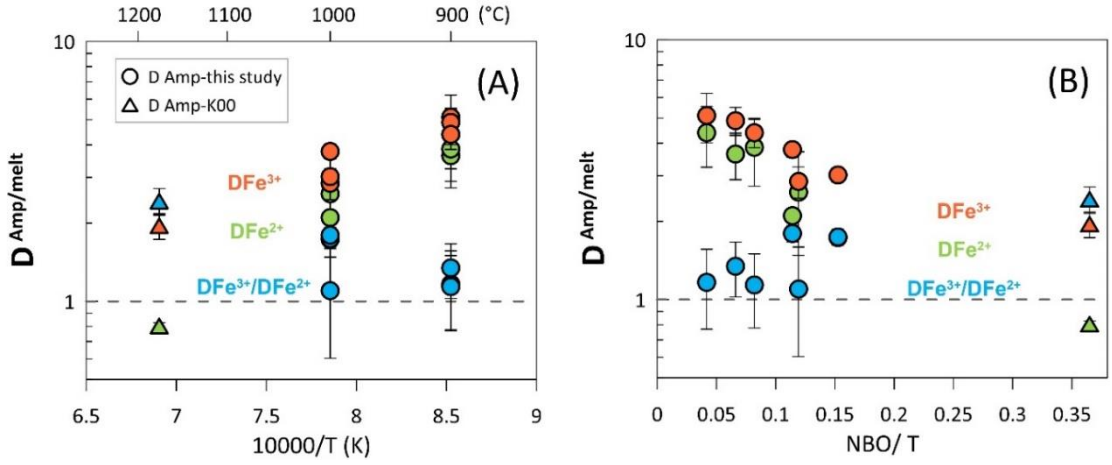

Fig. 4. DFe^{3+}, DFe^{2+} and DFe^{3+}/DFe^{2+} between amp and melt. (**A**) DFe^{3+}, DFe^{2+} and DFe^{3+}/DFe^{2+} as a function of 10000/T. (**B**) DFe^{3+}, DFe^{2+} and DFe^{3+}/DFe^{2+} as a function of melt NBO/T. K20 indicates D-values obtained from the most oxidizing experiments in King et al.[28].

The DFe_T, DFe^{2+}, DFe^{3+} and DFe^{3+}/DFe^{2+} for grt respectively ranges from 2.06 to 3.47, 4.49 to 10.29, 1.27 to 2.66 and 0.22 to 0.36 (Supplementary Table 4c). As highlighted by our and related manuscript's experiments, DFe_T, DFe^{2+} and DFe^{3+} decrease with T and melt NBO/T (Fig. 5A−B). But DFe^{3+}/DFe^{2+} is almost invariable (Fig. 5A−B) with an average of 0.33±0.06 (n=12).

$$\text{Grt: } DFe^{3+}/DFe^{2+}=0.33(\pm 0.06),\ n=12 \quad (8)$$

Contrary to cpx and amp, grt crystallization will increase Fe^{3+}/Fe_T and fO_2 of the residual melt because its DFe^{3+}/DFe^{2+} is always <1.

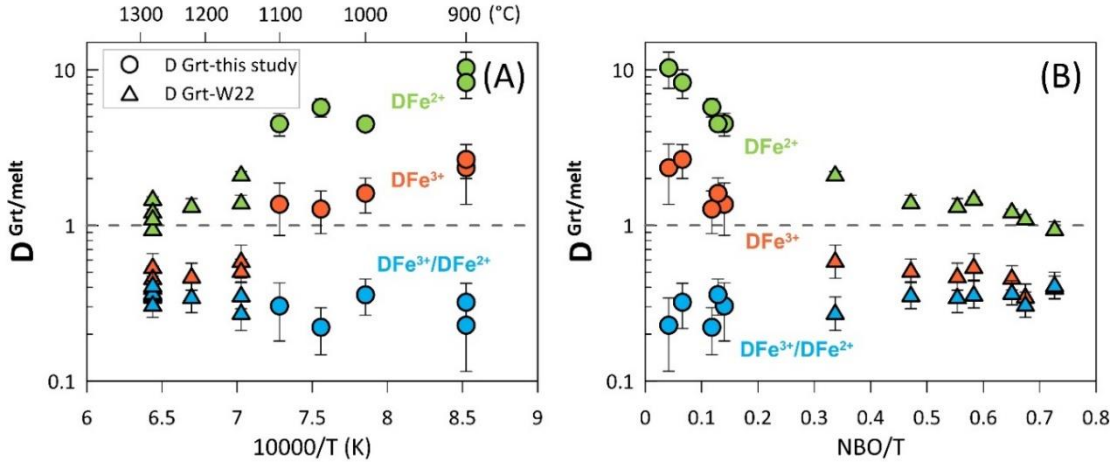

Fig. 5. DFe^{3+}, DFe^{2+} and DFe^{3+}/DFe^{2+} for grt and melt. (**A**) DFe^{3+}, DFe^{2+} and DFe^{3+}/DFe^{2+} as a function of 10000/T. (B) DFe^{3+}, DFe^{2+} and DFe^{3+}/DFe^{2+} as a function of NBO/T. References data cited are from W22: related manuscript.

In our experiments, mag shows values of 18.93−54.96 for DFe_T, 47.20−167.42 for DFe^{2+}, 14.94−42.46 for DFe^{3+} and 0.24−0.38 for DFe^{3+}/DFe^{2+} (Supplementary Table 4d). For spl, the DFe_T, DFe^{2+}, DFe^{3+} and DFe^{3+}/DFe^{2+} respectively range from 10.64 to 15.97, 8.29 to 19.55, 12.49 to 16.96 and 0.87 to 1.52 (Supplementary Table 4e). Consistent with literature data, DFe_T, DFe^{2+}, DFe^{3+} for both mag and spl decrease with T and melt NBO/T (Fig. 6). We also observed that the DFe^{3+}/DFe^{2+} for mag increases slightly with T and NBO/T, but the DFe^{3+}/DFe^{2+} for spl increases strongly with T and NBO/T (Fig. 6). Intriguingly, because the DFe^{3+}/DFe^{2+} is < 1 for mag and generally > 1 for spl, mag crystallization will elevate Fe^{3+}/Fe_T ratio and fO_2 of the residual melt, but spl crystallization has the opposite effect. The common view proposes that magnetite crystallization will decrease Fe^{3+}/Fe_T and fO_2 of the residual melt by assuming that magnetite contains abundant Fe^{3+} (Fe^{3+}: Fe^{2+}=2:1)[11,53]. On the contrary, our results reveal the opposite effect for mag crystallization because neither natural nor experimental mag is pure end member of Fe_3O_4[54]. Using the results from this study and related manuscript, the DFe^{3+}/DFe^{2+} for mag and spl can be regressed as the following equations:

$$\text{Mag: } DFe^{3+}/DFe^{2+}=0.9118-769.1/T,\ n=12,\ R^2=0.83 \quad (9)$$

$$\text{Spl: } DFe^{3+}/DFe^{2+}=9.7005-11142.3/T,\ n=17,\ R^2=0.79 \quad (10)$$

For the convenience of the redox modelling, we also regressed DFe^{2+} using T and obtained the following equations:

$$\text{Mag: Ln } DFe^{2+} = -5.0371 + 11832.8/T,\ n=12,\ R^2=0.93 \quad (11)$$

$$\text{Spl: Ln } DFe^{2+} = -7.4720 + 12918.7/T,\ n=17,\ R^2=0.95 \quad (12)$$

The high R^2 and low p-values (<0.05) demonstrate the reliability and accuracy of these regressions.

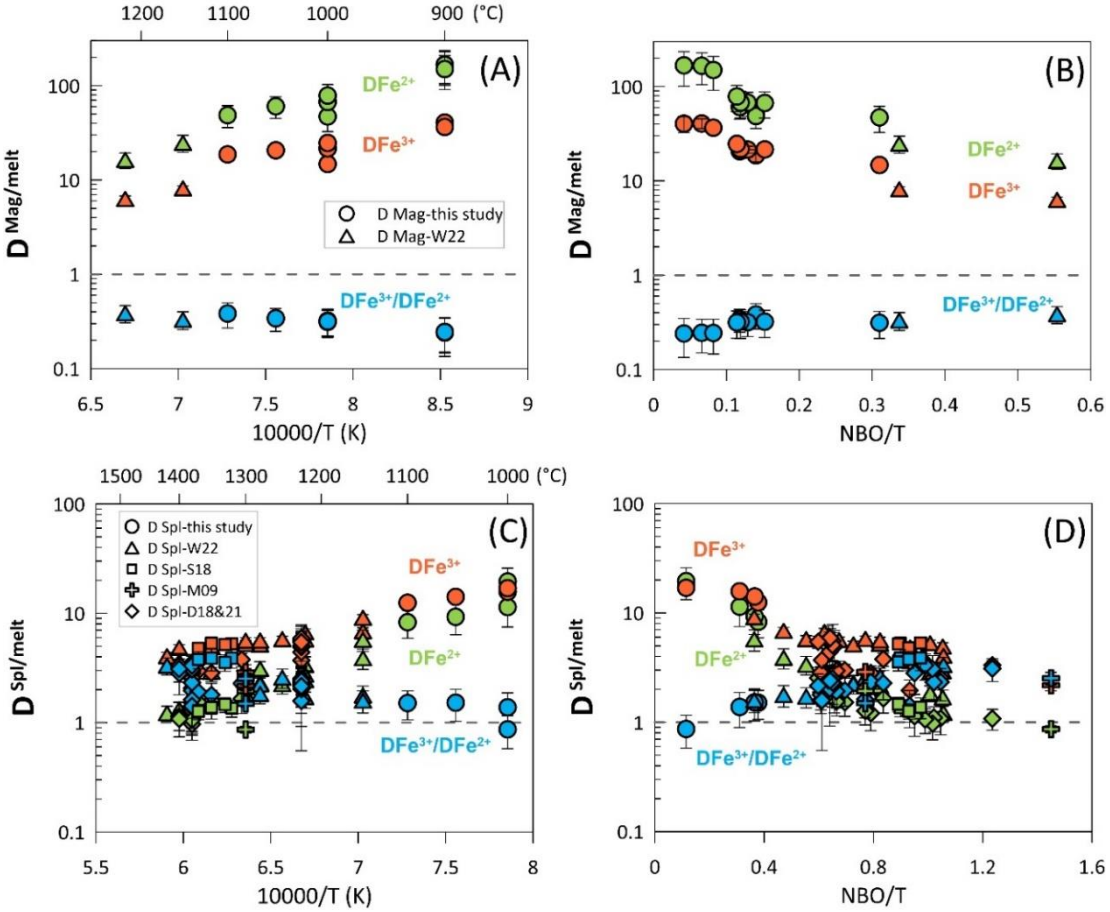

Fig. 6. DFe^{3+}, DFe^{2+} and DFe^{3+}/DFe^{2+} for Fe-oxides (mag and spl) and melt. (**A**) DFe^{3+}, DFe^{2+} and DFe^{3+}/DFe^{2+} as a function of 10000/T for mag. (**B**) DFe^{3+}, DFe^{2+} and DFe^{3+}/DFe^{2+} as a function of melt NBO/T for mag. (**C**) DFe^{3+}, DFe^{2+} and DFe^{3+}/DFe^{2+} as a function of 10000/T for spl. (**D**) DFe^{3+}, DFe^{2+} and DFe^{3+}/DFe^{2+} as a function of melt NBO/T for spl. References data are cited from W22: related manuscript, S18: Sorbadere et al.[52], M09: Mallmann & O'Neill[29] and D21: Davis et al.[21].

To summarize, DFe_T, DFe^{2+} and DFe^{3+} for silicate minerals and Fe-oxides all decrease with T and melt NBO/T. DFe^{3+}/DFe^{2+} for cpx decreases with T and NBO/T, but that for mag and spl increases with T and NBO/T. No obvious pressure effect on

313 DFe_T, DFe^{2+} and DFe^{3+} and DFe^{3+}/DFe^{2+} was observed. More importantly, the
314 crystallization of cpx, amp and spl will lower Fe^{3+}/Fe_T and fO_2 of the residual melt
315 because their DFe^{3+}/DFe^{2+} values are generally > 1. However, the crystallization of grt
316 and mag has an opposite effect because their DFe^{3+}/DFe^{2+} values are < 1. How the fO_2
317 evolves during arc magma differentiation should therefore depends on the crystallizing
318 mineral assemblages and the bulk mineral/melt partition coefficient of DFe^{3+} and
319 DFe^{2+}.

320 **Discussion**

321 **Redox evolution during arc magma differentiation**

322 The redox evolution during arc magma differentiation is dictated by Fe^{3+}/Fe_T of the
323 derivative melt. How Fe^{3+}/Fe_T of the melt changes depends on DFe^{3+}/DFe^{2+} of the
324 minerals and the crystallizing mineral assemblage. Here, we model the redox evolution
325 during arc magma differentiation by combining the determined DFe^{3+}/DFe^{2+} from this
326 study and the reported crystallizing mineral assemblages from Ulmer et al.[9]. Ulmer et
327 al.[9] experimentally determined the liquid line of descent (LLD) of typical primitive arc
328 magmas at 1 GPa using a high-Mg basalt and a high-Mg basaltic andesite, respectively.
329 Their experiments successfully reproduce the LLD of arc magmas and should mimic
330 the differentiation processes of arc magmas, which enable us to explore redox evolution
331 of typical arc magmas.

332 During arc magma differentiation, the Fe^{3+}/Fe^{2+} (i.e., Fe^{3+}/Fe_T) ratio of the melt
333 reflects the redox state of the magma, while the MgO content of the residual melt
334 records the degree of crystallinity. Therefore, we can investigate redox evolution during
335 magma differentiation by exploring how the melt Fe^{3+}/Fe_T ratio evolves with decreasing
336 melt MgO (Supplementary Table 5). At each differentiation step, MgO content and
337 Fe^{3+}/Fe_T ratio of the melt can be calculated from the bulk $D_{tot}Mg$, $D_{tot}Fe^{2+}$ and $D_{tot}Fe^{3+}$
338 between crystallizing minerals and residual melt. The bulk D-values of Mg, Fe^{2+} and
339 Fe^{3+} at each step are respectively weighted average of mineral DMg, DFe^{2+} and DFe^{3+}
340 and the mineral fraction. At a given step (in every 30 or 50 °C), the fraction of each
341 mineral is as reported in Ulmer et al. [9] and the DMg for each mineral can be calculated
342 from the MgO content of the experimental minerals and melt. DFe^{2+} for each mineral

at the step can then be derived from the calculated DMg according to Eqs. (3)−(5) or from the experimental temperature following Eqs. (11)−(12). After that, the DFe^{3+}/DFe^{2+} ratio for each mineral can be estimated from Eqs. (6)−(10) and thus DFe^{3+} can be determined from the derived DFe^{2+} and estimated DFe^{3+}/DFe^{2+}. For orthopyroxene, the DFe^{2+} was calculated from DMg using the regression in the related manuscript and the DFe^{3+}/DFe^{2+} were determined following the relation between DFe^{3+}/DFe^{2+}, temperature, and DAl (Supplementary Table 4f). For plagioclase, the DFe^{3+} and DFe^{2+} values were calculated based on the empirical equations from Lundgaard and Tegner[55].

Following the above rationale, we modelled the redox evolution during arc magma differentiation given an initial Fe^{3+}/Fe_T of 0.20 (±0.04), which is the average of the least degassed primitive arc basalts[15,56,57]. The fractional crystallization modelling for the high-Mg basalt and the high-Mg basaltic andesite is shown in Fig. 7. The details of the modelling are reported in Supplementary Table 5. As shown in Fig. 7, Fe^{3+}/Fe_T of the derivative melts shows limited variation during the differentiation of arc magmas. Specifically, during the differentiation of the high-Mg basalt, Fe^{3+}/Fe_T of the derivative melts ranges from 0.17−0.26, showing a slight decrease and an increase at MgO interval of 7.7−5.5 wt% and 3.9−3.4 wt%, respectively (Fig. 7A). The decrease in Fe^{3+}/Fe_T was induced by extensive crystallization of cpx and spl and the increase in Fe^{3+}/Fe_T was caused by mag crystallization. For the basaltic andesite, Fe^{3+}/Fe_T of the derivative melts range from 0.18−0.22 and is almost invariable during differentiation (Fig. 7B). The modelling results reproduce the observed $(Fe^{3+}/Fe_T)^{melt}$ from natural samples and indicate that the fO_2 of arc magmas remains invariable during differentiation[13-16,56,58]. Beneath thick crust, grt may fractionate and thus elevate Fe^{3+}/Fe_T of the residual melt[10]. However, recent studies demonstrated that arc magmas evolve mainly in the stability field of amp rather than grt, even for thick crust in Andes[59,60]. Therefore, our modelling results should represent a universal phenomenon considering that arc magmas evolve in a limited pressure range (amphibole stability field). We emphasize that although crystallization of a single mineral may elevate or lower Fe^{3+}/Fe_T and fO_2 of the residual

melt, the Fe^{3+}/Fe_T and fO_2 remain largely invariable because the fractionation capacities of the minerals on Fe^{3+}/Fe_T are counterbalanced.

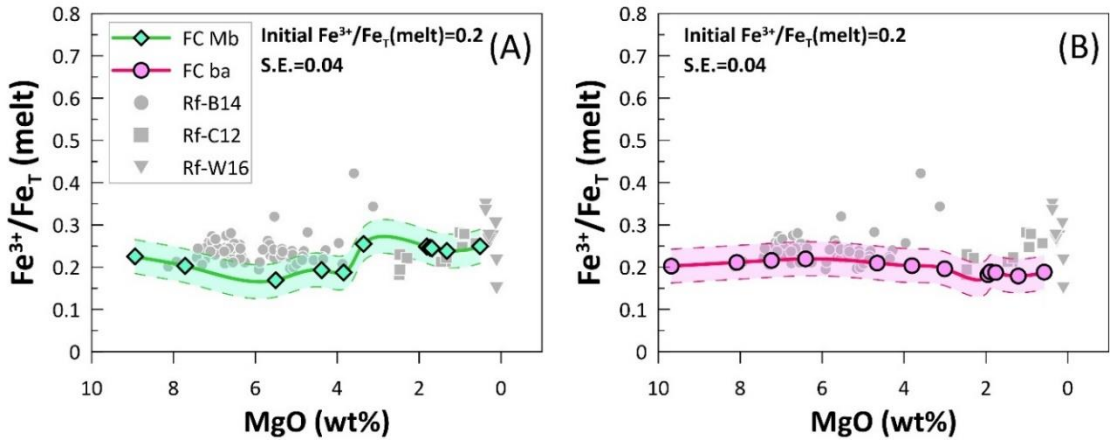

Fig. 7. Redox evolution of a high-Mg basalt (mb) and a high-Mg basaltic andesite (ba) revealed by Fe^{3+}/Fe_T of the derivative melts. (**A**) Redox evolution of a hydrous high-Mg basalt. (**B**) Redox evolution of a high-Mg basaltic andesite. The fractionation models are based on the LLD reported by Ulmer et al.[9]. Because our experiments and literature data cover a temperature range of 900−1420 °C, the redox modelling is restricted to ≥900 °C to avoid large uncertainties. Fe^{3+}/Fe_T ratios of the arc magmas are compiled from Brounce et al.[56], Crabtree and Lange[12] and Waters et al.[16].

Because the redox state of arc magmas barely changes during magmatic differentiation, the subaerial magmas and volcanic gases should inherit the redox state from mantle sources. Therefore, a well-reasoned inference could be: oxidizing volcanic gas must derive from an oxidized mantle. If the Great Oxidation Event (GOE) was triggered by increasing oxidizing capacity of volcanic gases[2,3], our results propose that the mantle must have become oxidized around the GOE as has also been proposed by other recent studies[4,61,62].

Methods

High pressure experiments

All the experiments were conducted at 1−2 GPa and 900−1100 °C on a piston cylinder apparatus at X. The starting material was a synthetic, medium-K basalt glass (MKBN2) containing 49.04 wt% SiO_2, 0.68 wt% TiO_2, 15.83 wt% Al_2O_3, 11.77 wt% FeO_T, 0.1 wt% MnO, 7.06 wt% MgO, 8.72 wt% CaO, 3.65 wt% Na_2O, 1.14 wt% K_2O, 0.20 wt% Cr_2O_3 and 0.10 wt% NiO. Another 0.7 wt% MnO and ~700ppm La was doped to this composition for other purpose. For each sample, we first loaded 5−10 wt% of H_2O followed by the Ru−RuO_2 mixture (the fO_2 buffer, Ru:RuO_2=1:1 wt%) at the bottom of the platinum (Pt) capsule (2.0 OD; 1.7 mm ID; 6 mm length). Then, ~6 mg starting material were filled into the Pt capsule, which was then welded shut. The mass ratio of the Ru−RuO_2 mixture and the starting material was adjusted to ~0.67. The use of the Ru−RuO_2 buffer maintains oxidizing conditions and prevents Fe loss during the experiments[18,31,41,63]. Besides, the Ru−RuO_2 buffer will not change the phase relations because Ru is relatively insoluble in silicate melts [<100 ppm,[41]]. Finally, the welded sample were checked for leaks by drying in an oven at 110 °C for more than 2 hours and then weighing. The Pt sample containers were then wrapped into a half-inch assembly and loaded into the piston cylinder. The experimental temperature was controlled by a thermos-controller and monitored by a Pt−$Pt_{90}Rh_{10}$ (S-type) thermocouple with an error of ± 2°C. Considering the temperature gradient, the temperature uncertainty of our experiments is within ± 15°C. A friction correction of 13% was applied for the 1/2 inch assembly and the pressure uncertainty is < 0.1 GPa. The experimental durations range from 75 to 126 hours, depending on the temperature (Supplementary Table 1). After the experiments, the samples were sectioned, mounted in epoxy resin, and polished for later backscattered electron imaging and electron microprobe analysis (EPMA).

EPMA analysis

The run products were observed under a Carl Zeiss SUPRA55 SAPPHIR field emission scanning electron microscope and analyzed using a JEOL JXA-8230 EPMA at X. The EPMA analytical conditions were set to an accelerating voltage of 15 kV, a beam current of 20 nA and a nominal 0 μm beam diameter for minerals. For quenched melts, the beam diameter was varied from 10−20 μm, depending on the size of the glass pools. Peak counting time was 10 s for all the elements; background counting time was 5 s. The primary standards were: olivine for Si; rutile for Ti; pyrope for Al; fayalite for Fe; bustamite for Mn; hornblende for Mg and Ca; orthoclase for K; and Albite for Na. Data reduction was performed by using a ZAF correction. A dry glass[64] was used as a secondary standard to monitor the analytical accuracy and precision. The recorded relative precision is better than ±2% for SiO_2, Al_2O_3, and CaO, ±5% for TiO_2, FeO, MnO, MgO, K_2O and ± 10% for Na_2O. The analytical results are reported in Supplementary Table 3.

Data availability

All data needed to evaluate the conclusions in the paper are present in the paper and/or the Supplementary information. Additional data related to this paper may be requested from the authors.

References

1 Gaillard, F., Scaillet, B. & Arndt, N. T. Atmospheric oxygenation caused by a change in volcanic degassing pressure. *Nature* **478**, 229-232, doi:10.1038/nature10460 (2011).

2 Holland, H. D. Volcanic gases, black smokers, and the Great Oxidation Event. *Geochimica Et Cosmochimica Acta* **66**, 3811-3826, doi:Pii S0016-7037(02)00950-X, doi 10.1016/S0016-7037(02)00950-X (2002).

3 Holland, H. D. Why the atmosphere became oxygenated: A proposal. *Geochimica et Cosmochimica Acta* **73**, 5241-5255, doi:10.1016/j.gca.2009.05.070 (2009).

4 Kadoya, S., Catling, D. C., Nicklas, R. W., Puchtel, I. S. & Anbar, A. D. Mantle data imply a decline of oxidizable volcanic gases could have triggered the Great Oxidation. *Nat Commun* **11**, 2774, doi:10.1038/s41467-020-16493-1 (2020).

5 Wallace, P. J. Volatiles in subduction zone magmas: concentrations and fluxes based on melt inclusion and volcanic gas data. *Journal of Volcanology and Geothermal Research* **140**, 217-240, doi:10.1016/j.jvolgeores.2004.07.023 (2005).

6 Zellmer, G. F., Edmonds, M. & Straub, S. M. Volatiles in subduction zone magmatism. *Geological Society, London, Special Publications* **410**, 1-17, doi:10.1144/sp410.13 (2015).

7 Annen, C., Blundy, J. D. & Sparks, R. S. J. The Genesis of Intermediate and Silicic Magmas in Deep Crustal Hot Zones. *Journal of Petrology* **47**, 505-539, doi:10.1093/petrology/egi084 (2006).

8 Lee, C.-T. A. & Bachmann, O. How important is the role of crystal fractionation in making intermediate magmas? Insights from Zr and P systematics. *Earth and Planetary Science Letters* **393**, 266-274, doi:10.1016/j.epsl.2014.02.044 (2014).

9 Ulmer, P., Kaegi, R. & Müntener, O. Experimentally Derived Intermediate to Silica-rich Arc Magmas by Fractional and Equilibrium Crystallization at 1·0 GPa: an Evaluation of Phase Relationships, Compositions, Liquid Lines of Descent and Oxygen Fugacity. *Journal of Petrology* **59**, 11-58, doi:10.1093/petrology/egy017 (2018).

10 Tang, M., Erdman, M., Eldridge, G. & Lee, C. A. The redox "filter" beneath magmatic orogens and the formation of continental crust. *Sci Adv* **4**, eaar4444, doi:10.1126/sciadv.aar4444 (2018).

11 Tang, M., Lee, C.-T. A., Costin, G. & Höfer, H. E. Recycling reduced iron at the base of magmatic orogens. *Earth and Planetary Science Letters* **528**, doi:10.1016/j.epsl.2019.115827 (2019).

12 Crabtree, S. M. & Lange, R. A. An evaluation of the effect of degassing on the oxidation state of hydrous andesite and dacite magmas: a comparison of pre- and post-eruptive Fe2+ concentrations. *Contributions to Mineralogy and Petrology* **163**, 209-224, doi:10.1007/s00410-011-0667-7 (2012).

13 de Hoog, J. C. M., Hattori, K. H. & Hoblitt, R. P. Oxidized sulfur-rich mafic magma at Mount Pinatubo, Philippines. *Contributions to Mineralogy and Petrology* **146**, 750-761, doi:10.1007/s00410-003-0532-4 (2003).

14 Grocke, S. B., Cottrell, E., de Silva, S. & Kelley, K. A. The role of crustal and eruptive processes versus source variations in controlling the oxidation state of iron in Central Andean magmas. *Earth and Planetary Science Letters* **440**, 92-104, doi:10.1016/j.epsl.2016.01.026 (2016).

15 Kelley, K. A. & Cottrell, E. The influence of magmatic differentiation on the oxidation state of Fe in a basaltic arc magma. *Earth and Planetary Science Letters* **329-330**, 109-121, doi:10.1016/j.epsl.2012.02.010 (2012).

16 Waters, L. E. & Lange, R. A. No effect of H2O degassing on the oxidation state of magmatic liquids. *Earth and Planetary Science Letters* **447**, 48-59, doi:10.1016/j.epsl.2016.04.030 (2016).

17 Kress, V. C. & Carmichael, I. S. E. The compressibility of silicate liquids containing Fe2O3 and the effect of composition, temperature, oxygen fugacity and pressure on their redox states. *Contributions to Mineralogy and Petrology* **108**, 82-92, doi:10.1007/BF00307328 (1991).

18 Zhang, H. L., Hirschmann, M. M., Cottrell, E. & Withers, A. C. Effect of pressure on Fe3+/ΣFe ratio in a mafic magma and consequences for magma ocean redox gradients. *Geochimica et Cosmochimica Acta* **204**, 83-103, doi:10.1016/j.gca.2017.01.023 (2017).

19 Carmichael, I. S. E. The redox states of basic and silicic magmas: a reflection of their source regions? *Contributions to Mineralogy and Petrology* **106**, 129-141, doi:10.1007/BF00306429 (1991).

20 Blundy, J. *et al.* Effect of redox on Fe–Mg–Mn exchange between olivine and melt and an oxybarometer for basalts. *Contributions to Mineralogy and Petrology* **175**, doi:10.1007/s00410-020-01736-7 (2020).

21 Davis, F. A. & Cottrell, E. Partitioning of Fe2O3 in peridotite partial melting experiments over a range of oxygen fugacities elucidates ferric iron systematics in mid-ocean ridge basalts and ferric iron content of the upper mantle. *Contributions to Mineralogy and Petrology* **176**, doi:10.1007/s00410-021-01823-3 (2021).

22 Davis, F. A., Humayun, M., Hirschmann, M. M. & Cooper, R. S. Experimentally determined mineral/melt partitioning of first-row transition elements (FRTE) during partial melting of peridotite at 3GPa. *Geochimica et Cosmochimica Acta* **104**, 232-260, doi:10.1016/j.gca.2012.11.009 (2013).

23 Ni, P., Zhang, Y., Fiege, A., Newville, M. & Lanzirotti, A. Rapid reduction of basaltic glasses in piston-cylinder experiments: a XANES study. *Contributions to Mineralogy and Petrology* **176**, doi:10.1007/s00410-021-01773-w (2021).

24 Takahashi, E. & Kushiro, I. Melting of a Dry Peridotite at High-Pressures and Basalt Magma Genesis. *American Mineralogist* **68**, 859-879 (1983).

514 25 Ulmer, P. The Dependence of the Fe-2+-Mg Cation-Partitioning between Olivine and Basaltic
515 Liquid on Pressure, Temperature and Composition - an Experimental-Study to 30 Kbars.
516 *Contributions to Mineralogy and Petrology* **101**, 261-273, doi:Doi 10.1007/Bf00375311
517 (1989).
518 26 Canil, D. & ONeill, H. S. C. Distribution of ferric iron in some upper-mantle assemblages.
519 *Journal of Petrology* **37**, 609-635, doi:DOI 10.1093/petrology/37.3.609 (1996).
520 27 Davis, F. A., Cottrell, E., Birner, S. K., Warren, J. M. & Lopez, O. G. Revisiting the electron
521 microprobe method of spinel-olivine-orthopyroxene oxybarometry applied to spinel
522 peridotitesk. *American Mineralogist* **102**, 421-435, doi:10.2138/am-2017-5823 (2017).
523 28 King, P. L., Hervig, R. L., Holloway, J. R., Delaney, J. S. & Dyar, M. D. Partitioning of
524 Fe3+/Fe-total between amphibole and basanitic melt as a function of oxygen fugacity. *Earth*
525 *and Planetary Science Letters* **178**, 97-112, doi:Doi 10.1016/S0012-821x(00)00071-6 (2000).
526 29 Mallmann, G. & O'Neill, H. S. C. The Crystal/Melt Partitioning of V during Mantle Melting as
527 a Function of Oxygen Fugacity Compared with some other Elements (Al, P, Ca, Sc, Ti, Cr, Fe,
528 Ga, Y, Zr and Nb). *Journal of Petrology* **50**, 1765-1794, doi:10.1093/petrology/egp053 (2009).
529 30 McCanta, M. C., Dyar, M. D., Rutherford, M. J. & Delaney, J. S. Iron partitioning between
530 basaltic melts and clinopyroxene as a function of oxygen fugacity. *American Mineralogist* **89**,
531 1685-1693, doi:DOI 10.2138/am-2004-11-1214 (2004).
532 31 Armstrong, K., Frost, D. J., McCammon, C. A., Rubie, D. C. & Ballaran, T. B. Deep magma
533 ocean formation set the oxidation state of Earth's mantle. **365**, 903-906,
534 doi:doi:10.1126/science.aax8376 (2019).
535 32 Cottrell, E. *et al.* A Mössbauer-based XANES calibration for hydrous basalt glasses reveals
536 radiation-induced oxidation of Fe. *American Mineralogist* **103**, 489-501, doi:10.2138/am-2018-
537 6268 (2018).
538 33 M. C. McCanta, M. D. D., C. Steven, M. Gunter, and A. Lanzirotti. In situ measurements of
539 Fe3+ in pyroxene using X-ray absorption spectroscopy: Using an oriented crystal calibration to
540 refine geothermobarometric calculations. (2018).
541 34 Li, L., Xiong, X. L. & Liu, X. C. Nb/Ta Fractionation by Amphibole in Hydrous Basaltic
542 Systems: Implications for Arc Magma Evolution and Continental Crust Formation. *Journal of*
543 *Petrology*, doi:10.1093/petrology/egw070 (2017).

35 Jones, J. H. Temperature-Independent and Pressure-Independent Correlations of Olivine Liquid Partition-Coefficients and Their Application to Trace-Element Partitioning. *Contributions to Mineralogy and Petrology* **88**, 126-132, doi:Doi 10.1007/Bf00371417 (1984).

36 Paul Beattie, C. F., Douglas Russell. Partition coefficients for olivine-melt and orthopyroxene-melt systems. (1991).

37 Adam, J. & Green, T. Trace element partitioning between mica- and amphibole-bearing garnet lherzolite and hydrous basanitic melt: 1. Experimental results and the investigation of controls on partitioning behaviour. *Contributions to Mineralogy and Petrology* **152**, 1-17, doi:10.1007/s00410-006-0085-4 (2006).

38 Tiepolo, M. *et al.* Nb and Ta incorporation and fractionation in titanian pargasite and kaersutite: crystal-chemical constraints and implications for natural systems. *Earth and Planetary Science Letters* **176**, 185-201, doi:Doi 10.1016/S0012-821x(00)00004-2 (2000).

39 O'Neill, H. S. C. & Nell, J. Gibbs free energies of formation of RuO 2 , IrO 2 , and OsO 2 : A high-temperature electrochemical and calorimetric study. *Geochimica et Cosmochimica Acta* **61**, 5279-5293, doi:10.1016/s0016-7037(97)00317-7 (1997).

40 Frost, B. R. Introduction to Oxygen Fugacity and Its Petrologic Importance. *Rev Mineral* **25**, 1-9 (1991).

41 O'Neill, H. S. C. *et al.* An experimental determination of the effect of pressure on the Fe3+/Sigma Fe ratio of an anhydrous silicate melt to 3.0 GPa. *American Mineralogist* **91**, 404-412, doi:10.2138/am.2005.1929 (2006).

42 Jayasuriya, K. D., O'Neill, H. S., Berry, A. J. & Campbell, S. J. A Mossbauer study of the oxidation state of Fe in silicate melts. *American Mineralogist* **89**, 1597-1609, doi:DOI 10.2138/am-2004-11-1203 (2004).

43 Borisov, A., Behrens, H. & Holtz, F. The effect of titanium and phosphorus on ferric/ferrous ratio in silicate melts: an experimental study. *Contributions to Mineralogy and Petrology* **166**, 1577-1591, doi:10.1007/s00410-013-0943-9 (2013).

44 O'Neill, H. S. C., Berry, A. J. & Mallmann, G. The oxidation state of iron in Mid-Ocean Ridge Basaltic (MORB) glasses: Implications for their petrogenesis and oxygen fugacities. *Earth and Planetary Science Letters* **504**, 152-162, doi:10.1016/j.epsl.2018.10.002 (2018).

45 Masotta, M. *et al.* The role of undercooling during clinopyroxene growth in trachybasaltic magmas: Insights on magma decompression and cooling at Mt. Etna volcano. *Geochimica et Cosmochimica Acta* **268**, 258-276, doi:10.1016/j.gca.2019.10.009 (2020).

46 Nandedkar, R. H., Ulmer, P. & Müntener, O. Fractional crystallization of primitive, hydrous arc magmas: an experimental study at 0.7 GPa. *Contributions to Mineralogy and Petrology* **167**, doi:10.1007/s00410-014-1015-5 (2014).

47 Neave, D. A. *et al.* Clinopyroxene–Liquid Equilibria and Geothermobarometry in Natural and Experimental Tholeiites: the 2014–2015 Holuhraun Eruption, Iceland. *Journal of Petrology* **60**, 1653-1680, doi:10.1093/petrology/egz042 (2019).

48 Welsch, B. *et al.* Clinopyroxene in postshield Haleakala ankaramite: 2. Texture, compositional zoning and supersaturation in the magma. *Contributions to Mineralogy and Petrology* **171**, doi:10.1007/s00410-015-1213-9 (2015).

49 Leake, B. E. *et al.* Nomenclature of amphiboles; report of the subcommittee on amphiboles of the International Mineralogical Association, Commission on New Minerals and Mineral Names. *The Canadian Mineralogist* **35**, 219-246 (1997).

50 Leake, B. E. *et al.* Nomenclature of amphiboles : additions and revisions to the International Mineralogical Association's amphibole nomenclature. *European Journal of Mineralogy* **16**, 191-196, doi:10.1127/0935-1221/2004/0016-0191 %J European Journal of Mineralogy (2004).

51 Ferracutti, G. R., Gargiulo, M. F., Ganuza, M. L., Bjerg, E. A. & Castro, S. M. Determination of the spinel group end-members based on electron microprobe analyses. *Mineralogy and Petrology* **109**, 153-160, doi:10.1007/s00710-014-0363-1 (2015).

52 Sorbadere, F. *et al.* The behaviour of ferric iron during partial melting of peridotite. *Geochimica et Cosmochimica Acta* **239**, 235-254, doi:10.1016/j.gca.2018.07.019 (2018).

53 Lee, C.-T. A. & Tang, M. How to make porphyry copper deposits. *Earth and Planetary Science Letters* **529**, doi:10.1016/j.epsl.2019.115868 (2020).

54 Richards, J. P. The oxidation state, and sulfur and Cu contents of arc magmas: implications for metallogeny. *Lithos* **233**, 27-45, doi:10.1016/j.lithos.2014.12.011 (2015).

55 Lundgaard, K. L. & Tegner, C. Partitioning of ferric and ferrous iron between plagioclase and silicate melt. *Contributions to Mineralogy and Petrology* **147**, 470-483, doi:10.1007/s00410-004-0568-0 (2004).

603 56 Brounce, M. N., Kelley, K. A. & Cottrell, E. Variations in Fe3+/∑Fe of Mariana Arc Basalts
604 and Mantle Wedge fO2. *Journal of Petrology* **55**, 2513-2536, doi:10.1093/petrology/egu065
605 (2014).
606 57 Kelley, K. A. & Cottrell, E. Water and the Oxidation State of Subduction Zone Magmas. **325**,
607 605-607, doi:doi:10.1126/science.1174156 (2009).
608 58 Wang, J., Xiong, X., Chen, Y. & Huang, F. Redox processes in subduction zones: Progress and
609 prospect. *Science China Earth Sciences* **63**, 1952-1968, doi:10.1007/s11430-019-9662-2
610 (2020).
611 59 Chen, W., Zhang, G., Ruan, M., Wang, S. & Xiong, X. Genesis of Intermediate and Silicic Arc
612 Magmas Constrained by Nb/Ta Fractionation. *Journal of Geophysical Research: Solid Earth*
613 **126**, doi:10.1029/2020jb020708 (2021).
614 60 Santana, L. C. V., McLeod, C. L., Blakemore, D., Shaulis, B. & Hill, T. Bolivian hornblendite
615 cumulates: Insights into the depths of Central Andean arc magmatic systems. *Lithos* **370**,
616 doi:ARTN 10561810.1016/j.lithos.2020.105618 (2020).
617 61 Aulbach, S. & Stagno, V. Evidence for a reducing Archean ambient mantle and its effects on
618 the carbon cycle. *Geology* **44**, 751-754, doi:10.1130/g38070.1 (2016).
619 62 Nicklas, R. W. *et al.* Secular mantle oxidation across the Archean-Proterozoic boundary:
620 Evidence from V partitioning in komatiites and picrites. *Geochimica et Cosmochimica Acta*
621 **250**, 49-75, doi:10.1016/j.gca.2019.01.037 (2019).
622 63 Wang, J., Xiong, X., Zhang, L. & Takahashi, E. Element loss to platinum capsules in high-
623 temperature–pressure experiments. *American Mineralogist* **105**, 1593-1597, doi:10.2138/am-
624 2020-7580 %J American Mineralogist (2020).
625 64 Xiong, X. L., Adam, J. & Green, T. H. Rutile stability and rutile/melt HFSE partitioning during
626 partial melting of hydrous basalt: Implications for TTG genesis. *Chemical Geology* **218**, 339-
627 359, doi:10.1016/j.chemgeo.2005.01.014 (2005).
628 65 Toplis, M. J. The thermodynamics of iron and magnesium partitioning between olivine and
629 liquid: criteria for assessing and predicting equilibrium in natural and experimental systems.
630 *Contributions to Mineralogy and Petrology* **149**, 22-39, doi:10.1007/s00410-004-0629-4
631 (2005).
632

Acknowledgments

Author contributions

Competing interests

The authors declare that they have no competing interests.

Additional information

Supplementary information is available for this paper.

Supplementary Files

This is a list of supplementary files associated with this preprint. Click to download.

- SupplementaryTables.xlsx
- SupplementaryInformation.docx